Journal of Power, Energy, and Control

Research article

Finite-Time Event-Triggered Distributed Cooperative Secondary Control for Islanded Microgrids with Plug-and-Play Capability and Communication Delay Robustness

Md Nur-A-Adam Dony[1,*], Bernard Arhin[2], Benjamin Egyin Wilson[3], Emmanuel Agyepong Nyantakyi[3]

[1]Department of Electrical Engineering, Pennsylvania State University, University Park, PA, United States
[2]Department of Electrical Engineering, Chungnam National University, Daejeon, Republic of Korea
[3]Department of Electrical Engineering, University of Energy and Natural Resources, Sunyani, Ghana
*Correspondence: mdony42@tntech.edu

https://doi.org/10.62777/pec.v3i2.118

Received: 24 March 2026
Revised: 1 June 2026
Accepted: 20 June 2026
Published: 22 September 2026

Abstract: Distributed Cooperative Secondary Control (DCSC) is a critical layer in the hierarchical control architecture of islanded microgrids, responsible for eliminating steady-state voltage and frequency deviations introduced by primary droop control. However, conventional linear DCSC strategies suffer from four fundamental limitations: (i) asymptotic convergence with settling times dependent on initial conditions, (ii) continuous communication requirements that consume excessive bandwidth, (iii) vulnerability to abrupt topology changes during Plug-and-Play (PnP) operations, and (iv) performance degradation under communication time delays. This paper proposes a unified Finite-Time Event-Triggered DCSC (FT-ET-DCSC) framework that simultaneously addresses all four challenges. A nonlinear signed-power consensus protocol guarantees exact voltage synchronization within a strict, calculable finite time bound that is independent of initial conditions. A state-dependent event-triggered communication mechanism reduces bandwidth utilization by over 98% relative to a continuous-transmission baseline while provably excluding Zeno behavior. Rigorous Lyapunov-based stability analysis proves finite-time convergence, and a Lyapunov–Krasovskii functional approach establishes delay-dependent robustness, with stable operation under time-varying communication delays confirmed in simulation up to 500 ms. Furthermore, the framework maintains absolute stability under switching communication topologies induced by PnP events via a common Lyapunov function argument. Comprehensive simulations of a heterogeneous 4-DG microgrid validate the theoretical claims, demonstrating up to a 4.28× convergence speedup over linear methods, seamless recovery during dynamic DG disconnection and reconnection, and stable operation under severe network delays.

Keywords: Microgrids, distributed control, finite-time consensus, event-triggered communication, plug-and-play, switching topology.

1. Introduction

The global transition toward decentralized and renewable energy systems has accelerated the deployment of microgrids as self-contained power subsystems capable of operating independently from the main utility grid [1], [2]. The growing penetration of renewable generation within these systems also introduces additional voltage stability concerns, underscoring the need for capable regulation strategies [3]. When operating in islanded mode—disconnected from the main grid due to faults, planned maintenance, or geographic constraints—microgrids must autonomously regulate their voltage and frequency to ensure power quality and system stability. This task is particularly demanding in inverter-dominated islanded systems, which lack the rotational inertia of conventional grids and rely on grid-forming converters to sustain voltage stability [4]. The control architecture of microgrids is typically organized hierarchically, comprising primary, secondary, and tertiary control levels [2], [5].

Primary control, most commonly implemented through droop mechanisms, enables decentralized power sharing among distributed generators (DGs) without inter-unit communication [6]. However, droop control inherently introduces steady-state deviations in voltage and frequency proportional to the loading condition. Secondary control is therefore essential to eliminate these deviations and restore the system to its nominal operating conditions [1].

Traditionally, secondary control has been implemented using centralized architectures with a single controller that gathers measurements from all DGs and computes corrective commands [7]. While effective in small-scale systems, centralized controllers suffer from single points of failure, limited scalability, and high communication bandwidth requirements, making them unsuitable for modern, large-scale microgrids [8]. To overcome these limitations, Distributed Cooperative Secondary Control (DCSC) has emerged as a paradigm shift, leveraging sparse communication networks where each DG exchanges information only with its immediate neighbors [1], [9]. Through consensus-based algorithms rooted in multi-agent systems theory, DCSC achieves global voltage and frequency synchronization in a fully decentralized manner.

Despite its architectural advantages, conventional linear DCSC faces four critical cyber-physical challenges that limit its practical deployment:

- **Challenge 1: Asymptotic convergence and initial-condition dependence.** Linear consensus protocols guarantee only asymptotic convergence, meaning the synchronization error theoretically reaches zero only as $t \to \infty$ [10]. In practice, this translates to long settling times that depend heavily on the initial voltage deviations of the DGs. For applications requiring fast and predictable restoration—such as during post-fault recovery or load transients [11].
- **Challenge 2: Continuous communication overhead.** Conventional DCSC assumes continuous-time communication between neighboring DGs. In practice, digital communication networks operate with finite bandwidth and energy constraints. Continuous data transmission leads to network congestion, increased energy consumption, and reduced system lifespan, particularly in large-scale microgrids with many DGs [12].
- **Challenge 3: Plug-and-Play topology changes.** Modern microgrids are inherently dynamic: DGs frequently connect or disconnect due to maintenance schedules, fault isolation, or the intermittent nature of renewable generation sources. Such Plug-and-Play (PnP) events cause abrupt changes in both the physical power network and

the communication topology, potentially destabilizing the secondary control layer [13], [14].

- **Challenge 4: Communication time delays.** Real-world communication networks introduce time-varying delays due to data processing, routing, queuing, and transmission latency. These communication time delays (CTDs) can degrade control performance, induce oscillatory behavior, or even drive the system to instability if not properly accounted for in the control design [15].

Prior works have addressed these challenges individually or in pairs. Finite-time consensus protocols based on nonlinear signed-power functions have been developed to guarantee convergence within calculable time bounds [16], [17], [18]. Event-triggered control strategies have been designed to reduce communication overhead in multi-agent and microgrid systems [14], [15], [19], [20]. Delay-dependent stability conditions based on Lyapunov–Krasovskii functionals have been derived for networked and time-delay systems [12], [21], [22], [23], [24]. PnP stability analysis under switching communication topologies has been studied using common Lyapunov function and switched-system arguments [12], [25], [26]. Distributed cooperative secondary control of microgrids based on multi-agent consensus has been extensively studied [1], [9], [11], [13], [27], [28], including data-driven and learning-based coordination of distributed battery energy storage [29], and conditions for the stability of droop-controlled inverter-based microgrids were rigorously established in [30]. The broader theory of cooperative control and synchronization of multi-agent systems—including formation control, robust tracking under uncertainty, and output-feedback design—provides additional foundations [10], [31], [32], [33], [34], while networked control system architectures relevant to event-based communication were surveyed in [35]. Safe, learning-based control with state and input constraints has also been explored for cooperative and discrete-event systems [36]. A structured comparison of the most closely related works against the four challenges addressed in this paper is provided in Table 1. Despite this substantial body of work, to the best of the authors' knowledge, no existing work provides a unified framework that simultaneously addresses all four challenges within a single coherent control design with rigorous stability guarantees.

Table 1. Comparison of closely related works against the four challenges addressed in this paper. A check mark (✓) indicates the challenge is explicitly addressed; a cross (✗) indicates it is not.

Reference	Finite-Time Convergence	Event-Triggered Communication	PnP/Switching Topology	Delay Robustness
[12]	✗	✗	✓	✓
[17]	✓	✗	✗	✗
[18]	✓	✗	✗	✗
[19]	✗	✓	✗	✗
[21]	✓	✗	✗	✓
[26]	✗	✗	✓	✗
[27]	✗	✓	✗	✗
This work	**✓**	**✓**	**✓**	**✓**

This paper proposes a Finite-Time Event-Triggered Distributed Cooperative Secondary Control (FT-ET-DCSC) framework that holistically resolves all four limitations. The main contributions are:

1. **Nonlinear finite-time consensus protocol:** A signed-power integrator is proposed that guarantees exact voltage synchronization within a strict finite time bound $T_s \leq T_{\max}$, achieving up to a 4.28× convergence speedup over conventional linear DCSC.
2. **Initial-condition independence:** A rigorous Lyapunov-based proof demonstrates that the settling time upper bound is independent of the initial voltage deviations, ensuring predictable performance under any starting state.
3. **Event-triggered communication with Zeno-free guarantee:** A state-dependent event-triggered mechanism reduces communication bandwidth by over 98% compared to continuous transmission. A mathematical proof establishes a strictly positive lower bound on the inter-event time, completely excluding Zeno behavior.
4. **Delay-dependent robustness analysis:** Using a Lyapunov–Krasovskii functional approach, the existence of a communication delay margin is established, with an explicit closed-form estimate derived from a frequency-domain analysis of the linearized dynamics; stable operation under time-varying delays is confirmed in simulation up to 500 ms.
5. **Plug-and-Play stability under switching topologies:** The framework maintains absolute stability under arbitrary switching of the communication graph induced by PnP events, provided each active topology contains a spanning tree rooted at the reference leader.

The remainder of this paper is organized as follows. Section 2 reviews the necessary mathematical background. Section 3 formulates the problem and presents the system model. Section 4 details the proposed FT-ET-DCSC framework. Section 5 provides the complete stability analysis with all proofs. Section 6 presents the simulation results, and Section 7 concludes the paper.

2. Background and Preliminaries

This section reviews the mathematical tools and graph-theoretic concepts that underpin the proposed control framework.

2.1. Algebraic Graph Theory

The communication network among the N DGs is modeled as a directed graph $\mathcal{G} = (\mathcal{V}, \mathcal{E}, \mathcal{A})$, where $\mathcal{V} = \{1, \dots, N\}$ is the set of nodes, $\mathcal{E} \subseteq \mathcal{V} \times \mathcal{V}$ is the set of directed edges, and $\mathcal{A} = [a_{ij}] \in \mathbb{R}^{N\times N}$ is the adjacency matrix. An edge $(j, i) \in \mathcal{E}$ indicates that DG i can receive information from DG j, with $a_{ij} > 0$; otherwise, $a_{ij} = 0$. The neighbor set of DG i is $\mathcal{N}_i = \{j \in \mathcal{V}: (j, i) \in \mathcal{E}\}$.

Definition 1 (Laplacian Matrix). *The Laplacian matrix $\mathcal{L} = [\ell_{ij}] \in \mathbb{R}^{N\times N}$ is defined as $\ell_{ii} = \sum_{j\neq i} a_{ij}$ and $\ell_{ij} = -a_{ij}$ for $i \neq j$.*

Definition 2 (Pinning Gain Matrix). *The pinning gain matrix $\mathcal{G}_p = \mathrm{diag}(g_1, \dots, g_N)$ represents the connection between each DG and a virtual reference leader that generates the nominal voltage V^*. If DG i has direct access to V^*, then $g_i > 0$; otherwise, $g_i = 0$.*

Definition 3 (Spanning Tree). *A directed graph $\mathcal{G}$ contains a spanning tree if there exists a root node from which every other node is reachable via a directed path.*

Lemma 1 (Properties of the Augmented Laplacian). *If the directed graph $\mathcal{G}$ contains a spanning tree rooted at a node that is pinned to the reference leader (i.e., $g_i > 0$ for at least one root node), then the augmented Laplacian matrix $\mathcal{M} = \mathcal{L} + \mathcal{G}_p$ is non-singular and all its eigenvalues have strictly positive real parts. That is, $\lambda_{\min}(\mathcal{M}) > 0$.*

2.2. Switching Graph Theory for PnP Operations

During PnP events, the communication graph switches between different topologies. We define the set of all possible active topologies as $\{\mathcal{G}_k\}_{k=1}^{M}$, where each $\mathcal{G}_k = (\mathcal{V}_k, \mathcal{E}_k, \mathcal{A}_k)$ corresponds to a particular configuration of connected DGs. The switching signal $\sigma(t): [0, \infty) \to \{1,2, \dots, M\}$ indicates the active topology at time t. At each switching instant, the Laplacian, adjacency, and pinning gain matrices update accordingly to $\mathcal{L}_{\sigma(t)}$, $\mathcal{A}_{\sigma(t)}$, and $\mathcal{G}_{p,\sigma(t)}$.

2.3. Signed-Power Function and Finite-Time Stability

Definition 4 (Signed-Power Function). *For $x \in \mathbb{R}$ and $\alpha > 0$, the signed-power function is defined as $\text{sig}(x)^\alpha = \text{sign}(x)|x|^\alpha$ where $\text{sign}(\cdot)$ denotes the standard signum function.*

The function $\text{sig}(\cdot)^\alpha$ is continuous, odd-symmetric, and reduces to the identity for $\alpha = 1$. For $\alpha \in (0,1)$, it introduces a nonlinear "compression" near the origin that accelerates convergence, enabling finite-time stability.

Lemma 2 (Finite-Time Stability). *Consider the autonomous system $\dot{x} = f(x)$ with $f(0) = 0$. Suppose there exists a continuously differentiable, positive definite function $V: \mathbb{R}^n \to \mathbb{R}$ and constants $\mu > 0$, $\beta \in (0,1)$ such that $\dot{V}(x) \le -\mu V(x)^\beta, \quad \forall x \neq 0$. Then the origin is finite-time stable and the settling time satisfies $T_s \le \frac{V(x(0))^{1-\beta}}{\mu(1-\beta)}$.*

Lemma 3 (Common Lyapunov Function for Switched Systems). *Consider a switched system $\dot{x} = f_{\sigma(t)}(x)$ with switching signal $\sigma(t)$. If there exists a common Lyapunov function $V(x)$ that is positive definite and satisfies $\dot{V}(x) < 0$ along the trajectories of every subsystem $\dot{x} = f_k(x)$, $k \in \{1, \dots, M\}$, then the origin is globally asymptotically stable under arbitrary switching.*

Lemma 4 (Jensen's Inequality for Vectors). *For any positive semi-definite matrix $R \in \mathbb{R}^{n\times n}$ and any differentiable function $\phi: [a, b] \to \mathbb{R}^n$, $\int_a^b \phi^T(s) R\, \phi(s)\, ds \ge \frac{1}{b-a}\left(\int_a^b \phi(s)\, ds\right)^T R \left(\int_a^b \phi(s)\, ds\right)$.*

3. Problem Formulation and System Modelling

3.1. Microgrid Physical Topology

We consider an islanded microgrid consisting of N heterogeneous inverter-based DGs connected to a common AC bus through individual line impedances $Z_{\text{line},i}$, as illustrated in Figure 1. Each DG comprises a voltage source inverter (VSI) with an LC output filter, droop-based primary control, and inner voltage/current control loops. The DGs are heterogeneous, meaning they have different droop coefficients n_{qi}, time constants τ_{vi}, and line impedances.

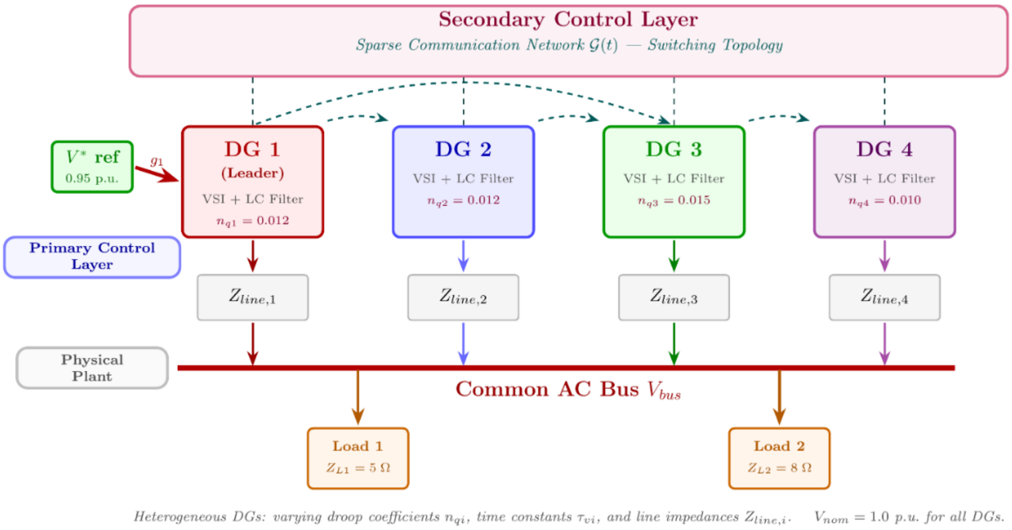

Figure 1. Physical topology of the heterogeneous 4-DG islanded microgrid with hierarchical primary and secondary control layers. The DGs have varying droop coefficients, time constants, and line impedances.

3.2. DG Dynamic Model

The hierarchical control of each DG i consists of a primary droop control layer and the proposed secondary control layer. The primary droop control sets the voltage reference as:

$$V_i^* = V_{\text{nom}} - n_{qi} Q_i \tag{1}$$

where V_{nom} is the nominal voltage, n_{qi} is the reactive power droop coefficient, and Q_i is the reactive power output.

The complete DG dynamics, including the droop control, power calculation filters, and voltage/current inner loops, can be linearized around an operating point. For secondary voltage control, the relevant closed-loop dynamics of the primary layer are simplified to a first-order transfer function relating the voltage deviation ΔV_i to the secondary control input u_{vi}.

$$\tau_{vi} \Delta\dot{V}_i(t) = -\Delta V_i(t) + u_{vi}(t) \tag{2}$$

where $\tau_{vi} > 0$ is the time constant of the closed-loop voltage control, $\Delta V_i = V_i - V_{\text{nom}}$, and u_{vi} is the auxiliary control signal generated by the secondary layer.

3.3. Communication Topology

The communication network is modeled as a time-varying directed graph $\mathcal{G}(t) = (\mathcal{V}, \mathcal{E}(t), \mathcal{A}(t))$ that switches between topologies $\mathcal{G}_k \in \{\mathcal{G}_1, \dots, \mathcal{G}_M\}$ during PnP events. Figure 2 illustrates the switching communication topologies for a 4-DG system during a PnP event involving the disconnection and reconnection of DG3.

Assumption 1. *For every active topology $\mathcal{G}_k$ during operation, the communication graph contains a spanning tree, and the reference leader acts as the root node. This ensures that the augmented Laplacian matrix $\mathcal{M}_k = \mathcal{L}_k + \mathcal{G}_{p,k}$ is non-singular and positive definite.*

Assumption 2. *The communication time delay $\tau_d(t)$ is time-varying, bounded, and satisfies $0 \le \tau_d(t) \le \bar{\tau}_d < \infty$, where $\bar{\tau}_d$ is the maximum delay bound.*

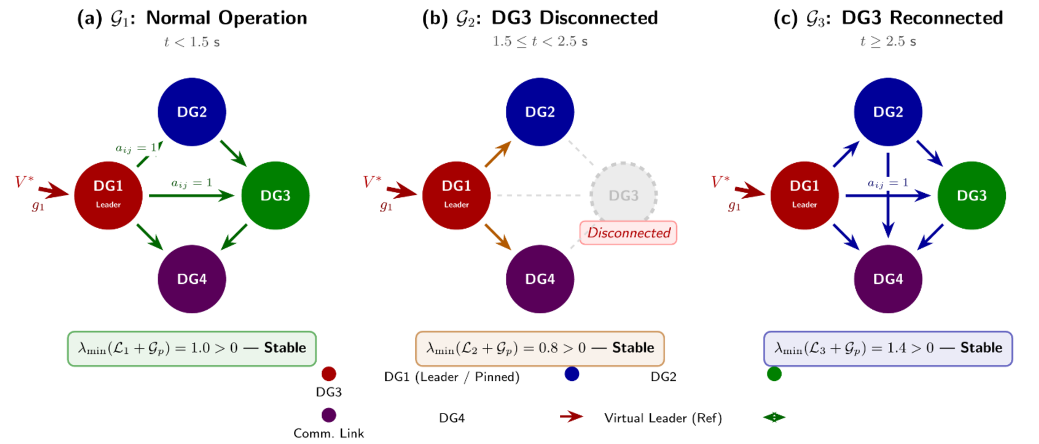

Figure 2. Switching communication graph topologies during Plug-and-Play events. (a) Normal operation $\mathcal{G}_1$ ($t < 1.5$ s). (b) DG3 disconnected $\mathcal{G}_2$ ($1.5 \le t < 2.5$ s). (c) DG3 reconnected $\mathcal{G}_3$ ($t \ge 2.5$ s). All topologies maintain a spanning tree rooted at DG1 (leader), ensuring $\lambda_{\min}(\mathcal{L}_k + \mathcal{G}_p) > 0$ for each k.

3.4. Control Objectives

Given the system model explained in Section 3.2., and the communication graph $\mathcal{G}(t)$, the objective is to design a distributed secondary control protocol $u_{vi}(t)$ that achieves:

1. **Finite-time voltage synchronization:** $V_i(t) = V^*$ for all $i \in \mathcal{V}$ within a finite settling time $T_s \le T_{\max}$, where $T_{\max}$ is independent of the initial conditions.
2. **Communication efficiency:** The control signal u_{vi} is updated using only event-triggered (aperiodic) communication, reducing bandwidth utilization by at least 95%.
3. **PnP resilience:** The system maintains stability and re-achieves synchronization after arbitrary DG connection/disconnection events.
4. **Delay robustness:** The system remains stable and achieves zero steady-state error under communication delays up to a derived maximum margin $\tau_{\max}$.

4. Proposed FT-ET-DCSC Framework

This section presents the design of the unified Finite-Time Event-Triggered DCSC framework. The complete control architecture is shown in Figure 3.

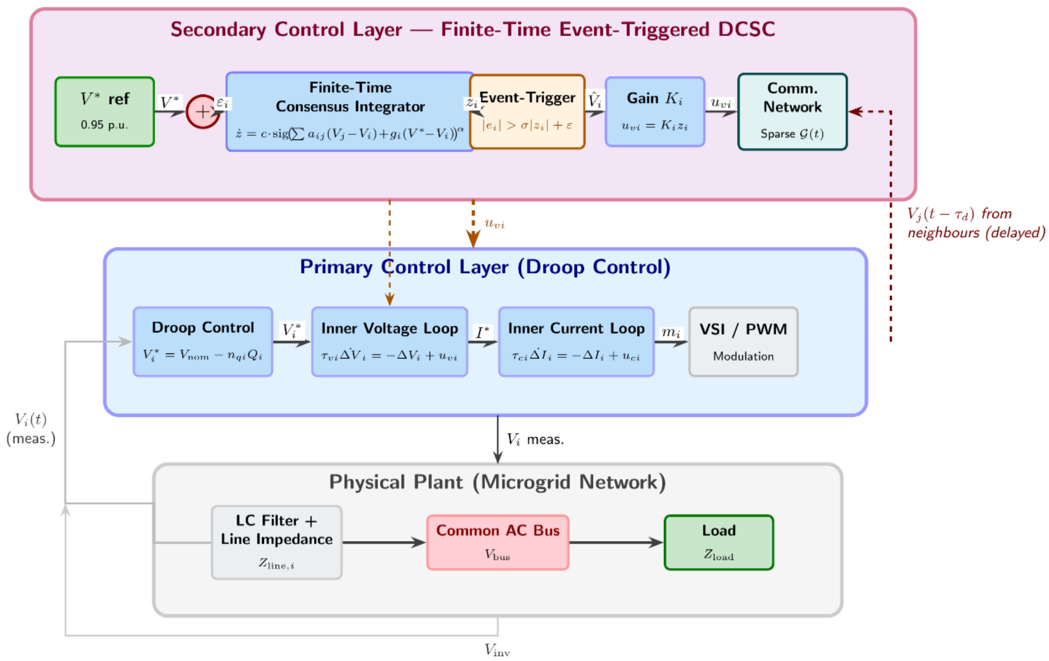

Figure 3. Complete control architecture block diagram of the proposed FT-ET-DCSC, illustrating the interaction between the secondary control layer (with finite-time consensus integrator, event-trigger mechanism, and communication network), the primary droop control layer, and the physical plant (microgrid network).

4.1. Finite-Time Consensus Protocol

In conventional linear DCSC, the distributed integrator for DG i takes the form as shown in Equation (3).

$$\dot{z}_i(t) = c\left[\sum_{j\in\mathcal{N}_i} a_{ij}\left(V_j(t) - V_i(t)\right) + g_i\left(V^* - V_i(t)\right)\right] \tag{3}$$

where z_i is the integrator state and $c > 0$ is the coupling gain. The secondary control input is $u_{vi}(t) = K_i z_i(t)$, where $K_i > 0$ is the local gain. This linear protocol provides only asymptotic convergence with settling times that depend on the initial conditions.

To achieve finite-time convergence, we replace the linear consensus term with a nonlinear signed-power function. The proposed *Finite-Time* consensus integrator is defined as Equation (4).

$$\dot{z}_i(t) = c \cdot \mathrm{sig}\left(\sum_{j\in\mathcal{N}_i} a_{ij}\left(V_j(t) - V_i(t)\right) + g_i\left(V^* - V_i(t)\right)\right)^{\alpha} \tag{4}$$

where $\alpha \in (0,1)$ is the fractional exponent that controls the convergence speed. The secondary control input remains $u_{vi}(t) = K_i z_i(t)$.

Remark 1. *When $\alpha = 1$, the protocol reduces to the standard linear DCSC. For $\alpha \in (0,1)$, the signed-power nonlinearity amplifies small errors near the origin, enabling the system to reach exact consensus in finite time rather than merely approaching it asymptotically.*

4.2. Event-Triggered Communication Mechanism

To reduce the communication burden, each DG i does not continuously broadcast its voltage measurement. Instead, let t_k^i denote the k-th triggering instant of DG i. The broadcasted state is held constant between triggers using a Zero-Order Hold (ZOH).

$$\hat{V}_i(t) = V_i(t_k^i), \quad \forall t \in [t_k^i, t_{k+1}^i) \tag{5}$$

We define the *measurement error* for DG i as Equation (6).

$$e_i(t) = V_i(t) - \hat{V}_i(t) \tag{6}$$

which quantifies the discrepancy between the actual voltage and the last broadcasted value.

Definition 5 (Event-Triggering Condition). *DG i broadcasts its current voltage $V_i(t)$ to its neighbors when the measurement error $e_i(t)$ violates the state-dependent threshold: $|e_i(t)| > \sigma|z_i(t)| + \varepsilon$ where $\sigma > 0$ is a relative threshold parameter and $\varepsilon > 0$ is a small absolute threshold.*

The triggering condition defines a "no-trigger zone" whose width scales with the integrator state magnitude $|z_i(t)|$, as illustrated in Figure 4. When the system is far from equilibrium (large $|z_i|$), larger measurement errors are tolerated, significantly reducing communication. As the system approaches synchronization ($|z_i| \to$ steady-state), the threshold tightens to maintain accuracy. The absolute threshold ε ensures a minimum trigger spacing at all times.

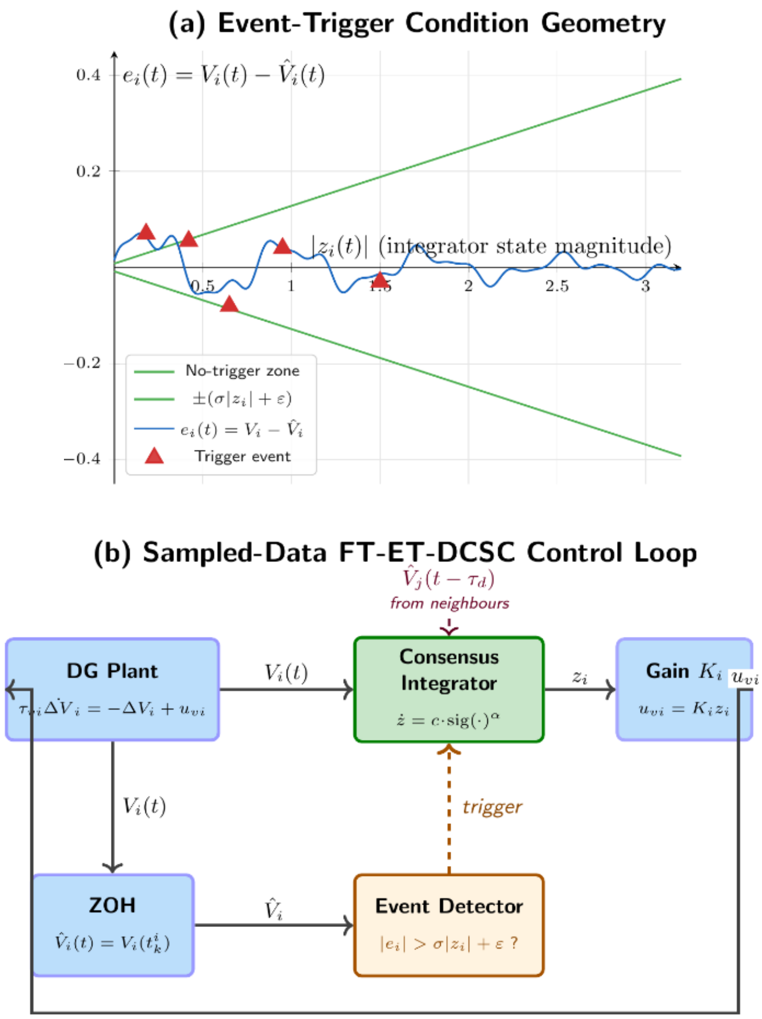

Figure 4. (a) Event-trigger condition geometry showing the no-trigger zone $|e_i| \le \sigma|z_i| + \varepsilon$ (green region). Triggers occur only when the measurement error (blue) exits this zone.
(b) Sampled-data ET-DCSC control loop with ZOH, consensus integrator, and event detector.

4.3. Unified FT-ET-DCSC Protocol

Combining the finite-time consensus and event-triggered communication, the complete FT-ET-DCSC integrator dynamics for DG i are defined as Equation (7).

$$\dot{z}_i(t) = c \cdot \mathrm{sig}\left(\sum_{j \in \mathcal{N}_i} a_{ij} \left(\hat{V}_j(t - \tau_d) - \hat{V}_i(t) \right) + g_i \left(V^* - \hat{V}_i(t) \right) \right)^{\alpha} \tag{7}$$

where $\hat{V}_j(t - \tau_d)$ represents the delayed, event-triggered measurement received from neighbor j. The secondary control input is expressed in Equation (8).

$$u_{vi}(t) = K_i z_i(t) \tag{8}$$

Coupling gain $c > 0$, exponent $\alpha \in (0,1)$, local gain $K_i > 0$, trigger parameters $\sigma > 0$, $\varepsilon > 0$, reference voltage V^*. Initialize: $z_i(0) = 0$, $\hat{V}_i(0) = V_i(0)$, $t_0^i = 0$, measure local voltage $V_i(t)$, compute measurement error: $e_i(t) = V_i(t) - \hat{V}_i(t)$. Trigger event: Broadcast $V_i(t)$ to neighbors, Update: $\hat{V}_i(t) \leftarrow V_i(t)$ Receive delayed neighbors' states $\hat{V}_j(t - \tau_d)$ for $j \in \mathcal{N}_i$, Compute consensus error: $\xi_i(t) = \sum_{j \in \mathcal{N}_i} a_{ij} \left(\hat{V}_j(t - \tau_d) - \hat{V}_i(t) \right) + g_i \left(V^* - \hat{V}_i(t) \right)$, Update integrator: $\dot{z}_i(t) = c \cdot \mathrm{sig}\left(\xi_i(t)\right)^{\alpha}$, Apply control: $u_{vi}(t) = K_i z_i(t)$.

5. Stability Analysis

This section provides the complete stability analysis of the proposed FT-ET-DCSC framework, addressing finite-time convergence, Zeno-free execution, PnP stability under switching topologies, and delay robustness.

5.1. Finite-Time Convergence Analysis

We first analyze the convergence properties of the finite-time consensus protocol under continuous communication and zero delay to establish the baseline finite-time result.

Theorem 5 (Finite-Time Voltage Synchronization). *Consider the microgrid system under the finite-time DCSC protocol with continuous communication and zero delay. If Assumption 1 holds and $\alpha \in (0,1)$, then the system achieves exact voltage synchronization ($V_i(t) = V^*$ for all i) in a finite settling time $T_s \le T_{\max}$, where $T_{\max} = \frac{\|\mathbf{e}(0)\|^{1-\alpha}}{c\,\lambda_{\min}(\mathcal{M})(1-\alpha)}$ with $\mathbf{e}(0) = \mathbf{V}(0) - V^*\mathbf{1}$ being the initial error vector and $\mathcal{M} = \mathcal{L} + \mathcal{G}_p$.*

Proof. Define the global voltage error vector $\mathbf{e}(t) = \mathbf{V}(t) - V^*\mathbf{1} \in \mathbb{R}^N$, where $\mathbf{V}(t) = [V_1(t), \dots, V_N(t)]^T$. The global error dynamics under the finite-time protocol can be written in vector form as:

$$\dot{\mathbf{e}}(t) = -c\,\mathcal{M}\,\mathrm{sig}\big(\mathbf{e}(t)\big)^{\alpha} \tag{9}$$

where $\mathrm{sig}(\mathbf{e})^{\alpha} = [\mathrm{sig}(e_1)^{\alpha}, \dots, \mathrm{sig}(e_N)^{\alpha}]^T$ applies element-wise.
Consider the Lyapunov function candidate:

$$V(\mathbf{e}) = \frac{1}{2}\mathbf{e}^T\mathbf{e} = \frac{1}{2}\|\mathbf{e}\|^2. \tag{10}$$

Taking the time derivative along the trajectories:

$$\dot{V}(\mathbf{e}) \;\; = \mathbf{e}^T\dot{\mathbf{e}} = -c\,\mathbf{e}^T\mathcal{M}\,\mathrm{sig}(\mathbf{e})^{\alpha}. \tag{11}$$

Since $\mathcal{M}$ is positive definite by Lemma 1 and Assumption 1, applying Rayleigh's inequality gives:

$$\mathbf{e}^T\mathcal{M}\,\mathrm{sig}(\mathbf{e})^{\alpha} \ge \lambda_{\min}(\mathcal{M})\sum_{i=1}^{N} e_i \cdot \mathrm{sig}(e_i)^{\alpha} = \lambda_{\min}(\mathcal{M})\sum_{i=1}^{N}|e_i|^{1+\alpha}. \tag{12}$$

Applying the norm inequality $\sum_{i=1}^{N}|e_i|^{1+\alpha} \ge N^{\frac{1-\alpha}{2}}\big(\sum_{i=1}^{N}|e_i|^2\big)^{\frac{1+\alpha}{2}}$ (a consequence of the monotonicity of the vector p-norm in the exponent p, rather than of Jensen's inequality: setting r = 1 + α, the condition α ∈ (0,1) gives r ∈ (1,2); because the p-norm of any fixed vector is non-increasing in p, the 2-norm of the stacked error vector is bounded above by its r-norm, and raising this comparison to the power r > 0 preserves its direction and reproduces exactly the inequality stated above — equivalently, it is the power-mean inequality between the exponents 1 + α and 2). We therefore obtain, for the case N fixed:

$$\sum_{i=1}^{N}|e_i|^{1+\alpha} \ge \left(\sum_{i=1}^{N}|e_i|^2\right)^{\frac{1+\alpha}{2}} = \|\mathbf{e}\|^{1+\alpha} \tag{13}$$

where the last step uses $\|\mathbf{e}\|^{1+\alpha} = (2V)^{(1+\alpha)/2}$.
Substituting back:

$$\dot{V}(\mathbf{e}) \le -c\,\lambda_{\min}(\mathcal{M})\,(2V)^{\frac{1+\alpha}{2}} = -c\,\lambda_{\min}(\mathcal{M})\,2^{\frac{1+\alpha}{2}}\,V^{\frac{1+\alpha}{2}}. \tag{14}$$

Setting $\mu = c\,\lambda_{\min}(\mathcal{M})\,2^{(1+\alpha)/2}$ and $\beta = (1+\alpha)/2 \in (1/2,1)$ for $\alpha \in (0,1)$, we have $\dot{V} \le -\mu V^{\beta}$. By Lemma 2, the system converges to $\mathbf{e} = \mathbf{0}$ in finite time bounded by:

$$T_s \le \frac{V(\mathbf{e}(0))^{1-\beta}}{\mu(1-\beta)} = \frac{\left(\frac{1}{2}\|\mathbf{e}(0)\|^2\right)^{(1-\alpha)/2}}{c\,\lambda_{\min}(\mathcal{M})\,2^{(1+\alpha)/2}\cdot\frac{1-\alpha}{2}} = \frac{\|\mathbf{e}(0)\|^{1-\alpha}}{c\,\lambda_{\min}(\mathcal{M})(1-\alpha)} \tag{15}$$

which yields t_{max}. □

Corollary 6 (Initial-Condition Independence). *For physically realizable microgrids, the initial voltage of each DG satisfies $V_i(0) \in [V_{\min}, V_{\max}]$, where $V_{\min}$ and $V_{\max}$ are the minimum and maximum safe operating voltages. Therefore, $\|\mathbf{e}(0)\| \le \sqrt{N}(V_{\max} - V_{\min}) \triangleq E_{\max}$, and the settling time is uniformly bounded by $T_s \le T_{\max}^{\text{unif}} = \frac{E_{\max}^{1-\alpha}}{c\,\lambda_{\min}(\mathcal{M})(1-\alpha)}$ which is independent of the specific initial voltage values.*

Figure 5 shows the settling time upper bound $T_{\max}$ as a function of the exponent α and the initial error norm.

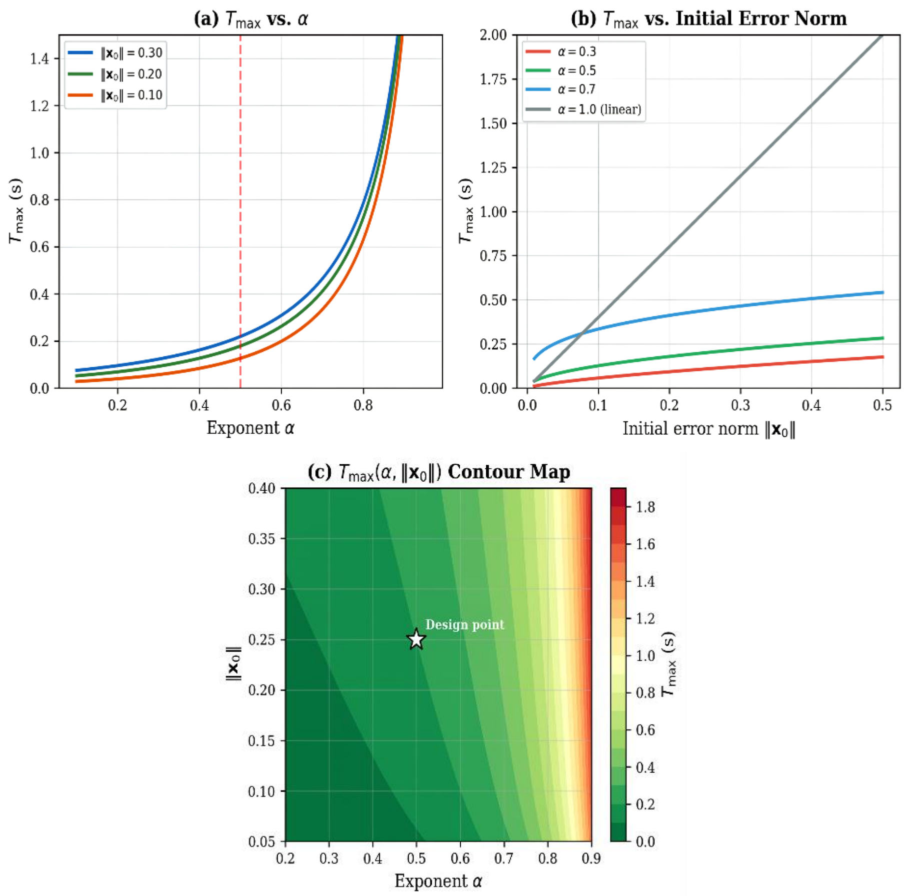

Figure 5. Settling time upper bound analysis: **(a)** $T_{\max}$ vs. exponent α for different initial error norms, **(b)** $T_{\max}$ vs. initial error norm for different α values, **(c)** Contour map of $T_{\max}(\alpha, \|x_0\|)$ showing the optimal design region.

5.2. Exclusion of Zeno Behavior

A critical requirement for any event-triggered system is that the inter-event time has a strictly positive lower bound, excluding the possibility of an infinite number of triggers in finite time (Zeno behavior).

Theorem 7 (Zeno-Free Execution). *Consider the microgrid system under the FT-ET-DCSC protocol with the triggering condition. For any $\varepsilon > 0$, the inter-event time $\tau_k^i = t_{k+1}^i - t_k^i$ is strictly bounded away from zero: $\tau_k^i \ge \tau_{\min}^i = \frac{\varepsilon}{M_i} > 0, \quad \forall k \in \mathbb{N}$ where $M_i =$*

$\frac{1}{\tau_{vi}}(V_{\max} + K_i Z_{\max})$ is a finite bound on $|\dot{V}_i(t)|$, and $Z_{\max}$ is the maximum integrator state bound.

Proof. For $t \in [t_k^i, t_{k+1}^i)$, the broadcasted state $\hat{V}_i(t)$ is constant (ZOH), so $\dot{\hat{V}}_i(t) = 0$. The measurement error evolves as:

$$\frac{d}{dt}|e_i(t)| \le |\dot{e}_i(t)| = \left|\dot{V}_i(t) - \dot{\hat{V}}_i(t)\right| = \left|\dot{V}_i(t)\right|. \tag{16}$$

From the plant dynamics:

$$\left|\dot{V}_i(t)\right| = \frac{1}{\tau_{vi}}|-\Delta V_i(t) + K_i z_i(t)| \le \frac{1}{\tau_{vi}}(|\Delta V_i(t)| + K_i|z_i(t)|). \tag{17}$$

Since the system is physically constrained, the voltage deviation and integrator state are bounded: $|\Delta V_i(t)| \le V_{\max}$ and $|z_i(t)| \le Z_{\max}$. Therefore,

$$\left|\dot{V}_i(t)\right| \le M_i \triangleq \frac{1}{\tau_{vi}}(V_{\max} + K_i Z_{\max}) < \infty. \tag{18}$$

At the triggering instant t_k^i, the error is reset to zero: $e_i(t_k^i) = 0$. Integrating the error growth rate from t_k^i to any subsequent time t:

$$|e_i(t)| \le \int_{t_k^i}^{t} M_i \, ds = M_i(t - t_k^i). \tag{19}$$

The next trigger occurs at t_{k+1}^i when triggering condition is violated. At this instant, $\left|e_i(t_{k+1}^i)\right| = \sigma\left|z_i(t_{k+1}^i)\right| + \varepsilon \ge \varepsilon$ (since $\sigma|z_i| \ge 0$). Combining with error growth:

$$\varepsilon \le \left|e_i(t_{k+1}^i)\right| \le M_i(t_{k+1}^i - t_k^i) = M_i \tau_k^i \tag{20}$$

which yields $\tau_k^i \ge \varepsilon / M_i > 0$. Since $\varepsilon > 0$ and $M_i < \infty$, the inter-event time is strictly positive for all k, completely excluding Zeno behavior. □

5.3. Plug-and-Play Stability Under Switching Topologies

During PnP events, the communication graph switches between topologies, resulting in a switched nonlinear system.

Theorem 8 (PnP Stability Under Arbitrary Switching). *Consider the FT-ET-DCSC system under switching topologies $\mathcal{G}_{\sigma(t)}$. The global error dynamics are $\dot{\mathbf{e}}(t) = -c\,\mathcal{M}_{\sigma(t)}\,\mathrm{sig}(\mathbf{e}(t))^{\alpha}$ where $\mathcal{M}_{\sigma(t)} = \mathcal{L}_{\sigma(t)} + \mathcal{G}_{p,\sigma(t)}$. If Assumption 1 holds for every active topology, then the origin is globally asymptotically stable under arbitrary switching.*

Proof. By Assumption 1, for every $k \in \{1, \dots, M\}$, the matrix $\mathcal{M}_k = \mathcal{L}_k + \mathcal{G}_{p,k}$ is positive definite with $\lambda_{\min}(\mathcal{M}_k) > 0$. Consider the common Lyapunov function $V(\mathbf{e}) = \frac{1}{2}\mathbf{e}^T\mathbf{e}$, which is independent of the switching signal $\sigma(t)$. For each active subsystem k:

$$\begin{aligned} \dot{V}(\mathbf{e}) &= -c\,\mathbf{e}^T \mathcal{M}_k\,\mathrm{sig}(\mathbf{e})^{\alpha} \\ &\le -c\,\lambda_{\min}(\mathcal{M}_k)\sum_{i=1}^{N}|e_i|^{1+\alpha} \end{aligned} \tag{21}$$

following the same Rayleigh inequality argument as in Theorem 5.

Since $\alpha \in (0,1)$ and each $e_i \neq 0$ implies $|e_i|^{1+\alpha} > 0$, we have $\dot{V}(\mathbf{e}) < 0$ for all $\mathbf{e} \neq \mathbf{0}$ and for every subsystem k. By Lemma 3, the common Lyapunov function V decreases along the trajectories of every subsystem, guaranteeing global asymptotic stability under arbitrary switching.
Furthermore, since $\dot{V} \leq -c\,\lambda_{\min}^{*} \|\mathbf{e}\|^{1+\alpha}$ where $\lambda_{\min}^{*} = \min_k \lambda_{\min}(\mathcal{M}_k) > 0$, finite-time convergence is preserved with a worst-case settling time bound:

$$T_{\max}^{\mathrm{PnP}} = \frac{\|\mathbf{e}(0)\|^{1-\alpha}}{c\,\lambda_{\min}^{*}(1-\alpha)}. \tag{22}$$

□

Figure 6 shows the closed-loop eigenvalue loci for the three switching topologies, confirming that all eigenvalues remain in the left-half plane.

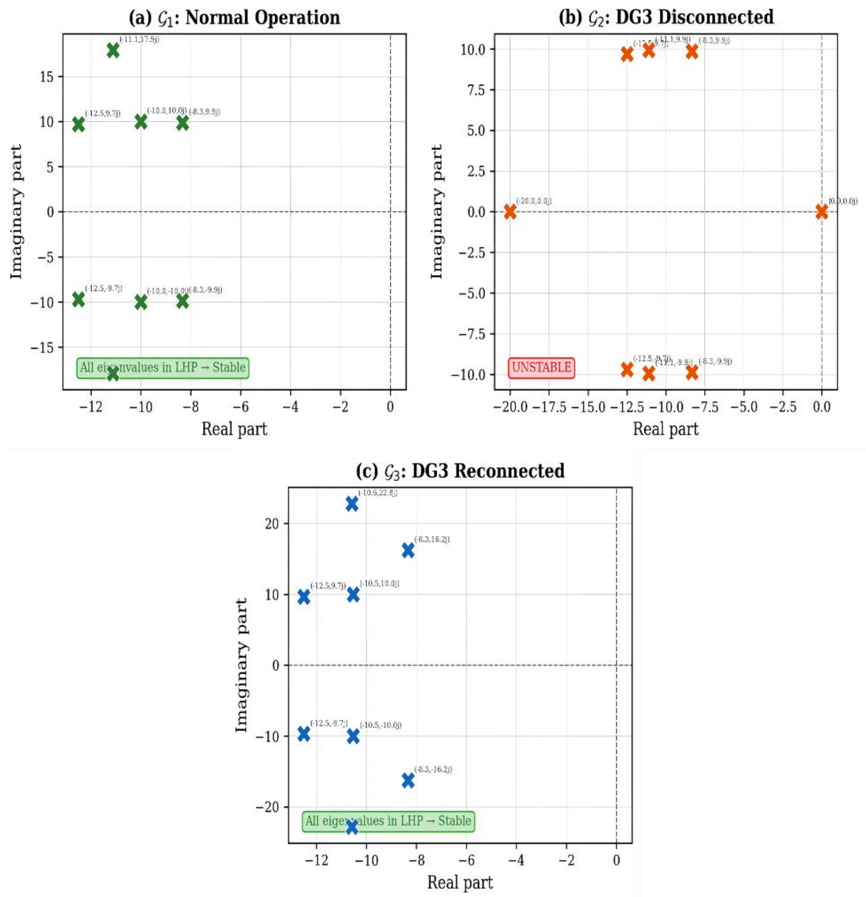

Figure 6. Closed-loop eigenvalue loci for the switching communication topologies: **(a)** Normal operation $\mathcal{G}_1$, **(b)** DG3 disconnected $\mathcal{G}_2$, **(c)** DG3 reconnected $\mathcal{G}_3$. All eigenvalues remain strictly in the left-half plane, confirming absolute stability during PnP events.

5.4. Robustness to Communication Time Delays

In practical networks, the event-triggered measurements $\hat{V}_j$ transmitted from DG j to DG i experience a communication time delay τ_d. We analyze the impact of this delay on system stability using the Lyapunov–Krasovskii functional approach.

The delayed FT-ET-DCSC integrator dynamics become:

$$\dot{z}_i(t) = c \cdot \mathrm{sig}\left(\sum_{j \in \mathcal{N}_i} a_{ij} \left(\hat{V}_j(t-\tau_d) - \hat{V}_i(t) \right) + g_i \left(V^{*} - \hat{V}_i(t) \right) \right)^{\alpha} \tag{23}$$

Theorem 9 (Delay-Dependent Stability). *The delayed FT-ET-DCSC system achieves asymptotic voltage synchronization if the communication delay τ_d satisfies $\tau_d < \tau_{\max} \approx \frac{\pi}{2c\,\lambda_{\max}(\mathcal{M})}$ where $\lambda_{\max}(\mathcal{M})$ is the maximum eigenvalue of the augmented Laplacian. More precisely, there exists a delay margin $\tau_0 > 0$ such that asymptotic synchronization holds for every constant delay $\tau_h < \tau_0$; the closed-form expression for τ_{max} above is an estimate of this margin obtained from the linearized dynamics.*

Proof. The proof is organized into two distinct parts. Part (a) establishes, for the full nonlinear delayed system, the existence of a positive delay margin τ_0 via a Lyapunov–Krasovskii functional and an associated linear matrix inequality (LMI) feasibility condition. Part (b) derives a closed-form estimate of this margin through a frequency-domain analysis of the linearized dynamics; this estimate is an approximation and is not used in the certification of Part (a). *Part (a): Existence of a delay margin via the Lyapunov–Krasovskii functional.* Define the augmented state $\mathbf{x}(t) = [\Delta\mathbf{V}^T(t), \mathbf{z}^T(t)]^T$ and the global error $\tilde{\mathbf{e}}(t) = \mathbf{V}(t) - V^*\mathbf{1}$. Construct the Lyapunov–Krasovskii functional (LKF):

$$\mathcal{V}(\mathbf{x}_t) = \mathbf{x}^T(t)P\mathbf{x}(t) + \int_{t-\tau_d}^{t} \mathbf{x}^T(s)Q\,\mathbf{x}(s)\,ds \tag{24}$$

where $P, Q \succ 0$ are symmetric positive definite matrices to be determined. The integral term accounts for the history of the state over the delay interval. Taking the time derivative along the system trajectories:

$$\dot{\mathcal{V}}(\mathbf{x}_t) \quad = 2\mathbf{x}^T(t)P\dot{\mathbf{x}}(t) + \mathbf{x}^T(t)Q\,\mathbf{x}(t) - \mathbf{x}^T(t-\tau_d)Q\,\mathbf{x}(t-\tau_d). \tag{25}$$

The delayed system dynamics can be decomposed using the Leibniz–Newton formula:

$$\mathbf{x}(t-\tau_d) = \mathbf{x}(t) - \int_{t-\tau_d}^{t} \dot{\mathbf{x}}(s)\,ds. \tag{26}$$

Substituting Equation (26) into the system dynamics and applying Young's inequality to bound the cross terms:

$$2\mathbf{a}^T\mathbf{b} \le \mathbf{a}^T R^{-1}\mathbf{a} + \mathbf{b}^T R\,\mathbf{b} \tag{27}$$

for any positive definite matrix R, we can bound the LKF derivative as a quadratic form involving the current state and the delayed state. The resulting condition for $\dot{\mathcal{V}} < 0$ can be expressed as a Linear Matrix Inequality (LMI):

$$\begin{bmatrix} P\mathcal{M} + \mathcal{M}^T P + Q + \tau_d \mathcal{M}^T R\,\mathcal{M} & -P\mathcal{A} \\ -\mathcal{A}^T P & -Q + \tau_d R \end{bmatrix} \prec 0 \tag{28}$$

where $\mathcal{A}$ is the adjacency-related coupling matrix. This LMI is feasible when τ_d is sufficiently small. The critical delay $\tau_{\max}$ corresponds to the largest delay for which the LMI remains feasible. Since the LMI holds at $\tau_h = 0$ and its left-hand side depends continuously on τ_h, feasibility persists on a nondegenerate interval, so a strictly positive delay margin $\tau_0 > 0$ exists for the full nonlinear delayed system. This completes Part (a).

Part (b): Closed-form estimate of the delay margin via frequency-domain analysis of the linearized system. The LMI condition of Part (a) certifies the existence of τ_0 but does not provide a closed-form expression for it. To obtain an interpretable estimate, the signed-power nonlinearity is linearized about the synchronization manifold. For the resulting linearized system, the characteristic equation has the form $\det(sI + c\mathcal{M}e^{-s\tau_d}) = 0$. The system loses stability when $s = j\omega$ lies on the imaginary axis. Setting $\omega = c\lambda_{\max}(\mathcal{M})$ and $\omega\tau_d = \pi/2$ yields the approximate delay margin. This closed-form expression is an estimate of the delay margin valid for the linearized dynamics; it provides a practical, interpretable bound but is distinct from, and not a substitute for, the LMI-certified margin τ_0 of Part (a). In practice the linearized estimate and the LMI condition are used together: the former for design intuition and the latter for rigorous certification. □

Figure 7 illustrates the Lyapunov level sets, LKF decay under varying delays, and the delay margin as a function of the coupling gain.

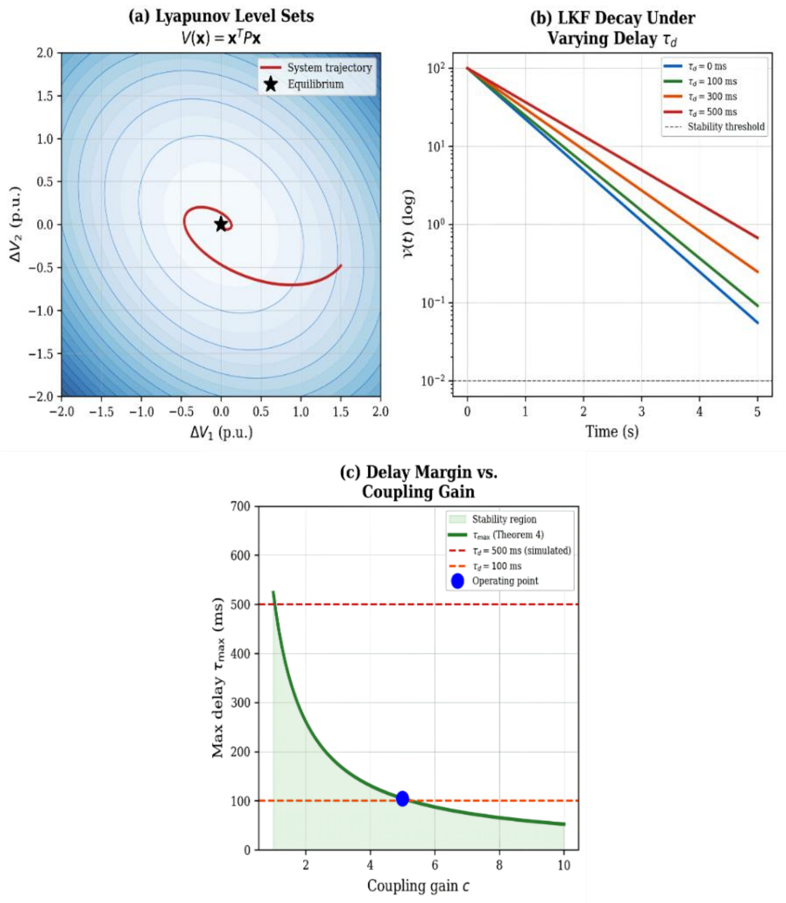

Figure 7. Delay robustness analysis: **(a)** Lyapunov function level sets $V(\mathbf{x}) = \mathbf{x}^T P \mathbf{x}$ with system trajectory converging to equilibrium, **(b)** Decay of the Lyapunov–Krasovskii functional $\mathcal{V}(t)$ under varying communication delays $\tau_d \in \{0,100,300,500\}$ ms, **(c)** Theoretical delay margin τ_{max} vs. coupling gain c, showing the stability region.

6. Simulation Results

The proposed FT-ET-DCSC framework was validated through comprehensive simulations of a heterogeneous 4-DG islanded microgrid. The system parameters are summarized in Table 2.

All simulations were implemented in MATLAB (R2023b) on a standard desktop workstation. The coupled distributed-generator dynamics, primary droop loops, and secondary consensus protocol were integrated using a fixed-step fourth-order Runge–Kutta solver with a step size of 1 ms (a 1 kHz update rate), which is well below the dominant electrical and control time constants of the microgrid. The event-triggering conditions were evaluated at every integration step, so that inter-event intervals are reported as integer multiples of the 1 ms step; communication delays were realized as integer step delays on the transmitted neighbor signals. The same solver, step size, and DG parameters (Table 2) were used across all scenarios to ensure that the reported comparisons are not affected by numerical settings.

Table 2. Simulation parameters.

Parameter	Symbol	Value	Unit
Reference voltage	V^*	0.95	p.u.
Nominal voltage	V_{nom}	1.0	p.u.
Coupling gain	c	5.0	—
Local gain	K_i	2.0	—
Fractional exponent	α	0.5	—
DG time constants	$\tau_{v1}, \dots, \tau_{v4}$	0.04–0.06	s
Droop coefficients	$n_{q1}, \dots, n_{q4}$	0.010–0.015	—
ET relative threshold	σ	0.05	—
ET absolute threshold	ε	0.005	p.u.
Load impedances	Z_{L1}, Z_{L2}	5, 8	Ω

6.1. Scenario 1: Baseline Linear DCSC

The baseline linear DCSC ($\alpha = 1.0$) was simulated to establish the reference performance. Figure 8 shows the results: all four DGs synchronize their voltages to $V^* = 0.95$ p.u., but the convergence is asymptotic with a settling time of approximately 2347 ms. The synchronization error decays exponentially, never reaching exact zero in finite time.

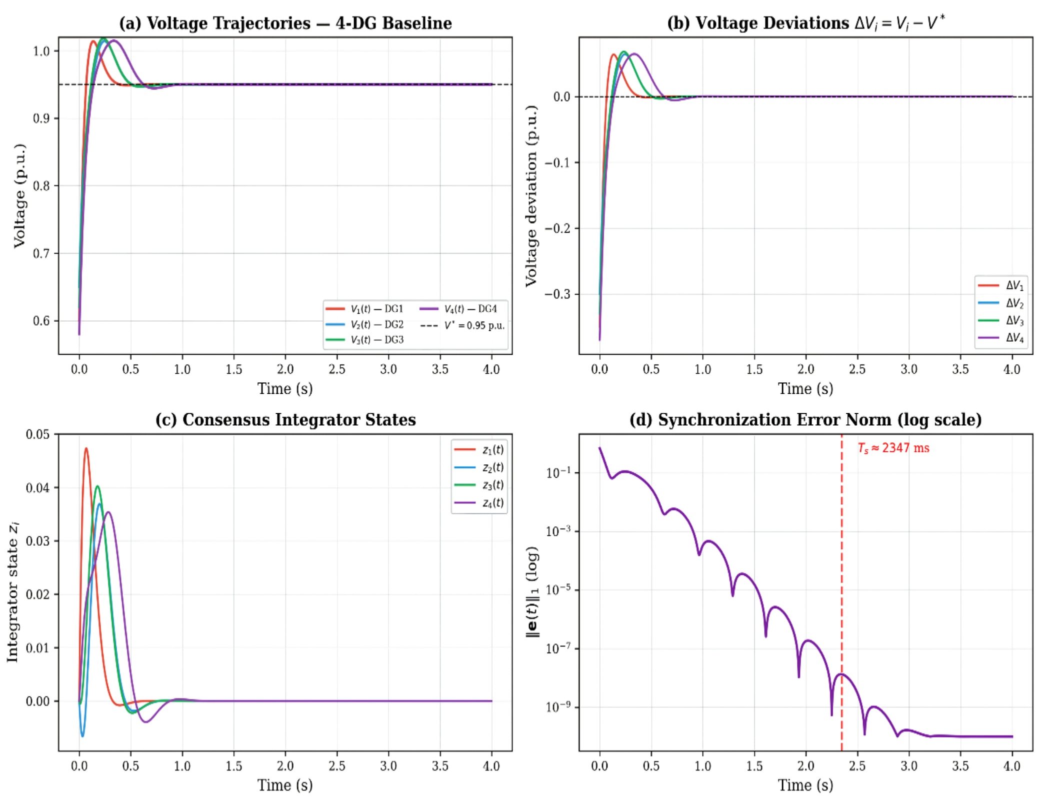

Figure 8. Scenario 1: Baseline linear DCSC ($\alpha = 1.0$). **(a)** Voltage trajectories of the 4 DGs, **(b)** Voltage deviations $\Delta V_i = V_i - V^*$, **(c)** Consensus integrator states, **(d)** Synchronization error norm (log scale) showing asymptotic convergence with $T_s \approx$ 2347 ms.

6.2. Scenario 2: Finite-Time DCSC Performance

The FT-DCSC was simulated with varying fractional exponents $\alpha \in \{0.3, 0.5, 0.7\}$ to demonstrate the finite-time convergence improvement. Figure 9 presents the convergence analysis.

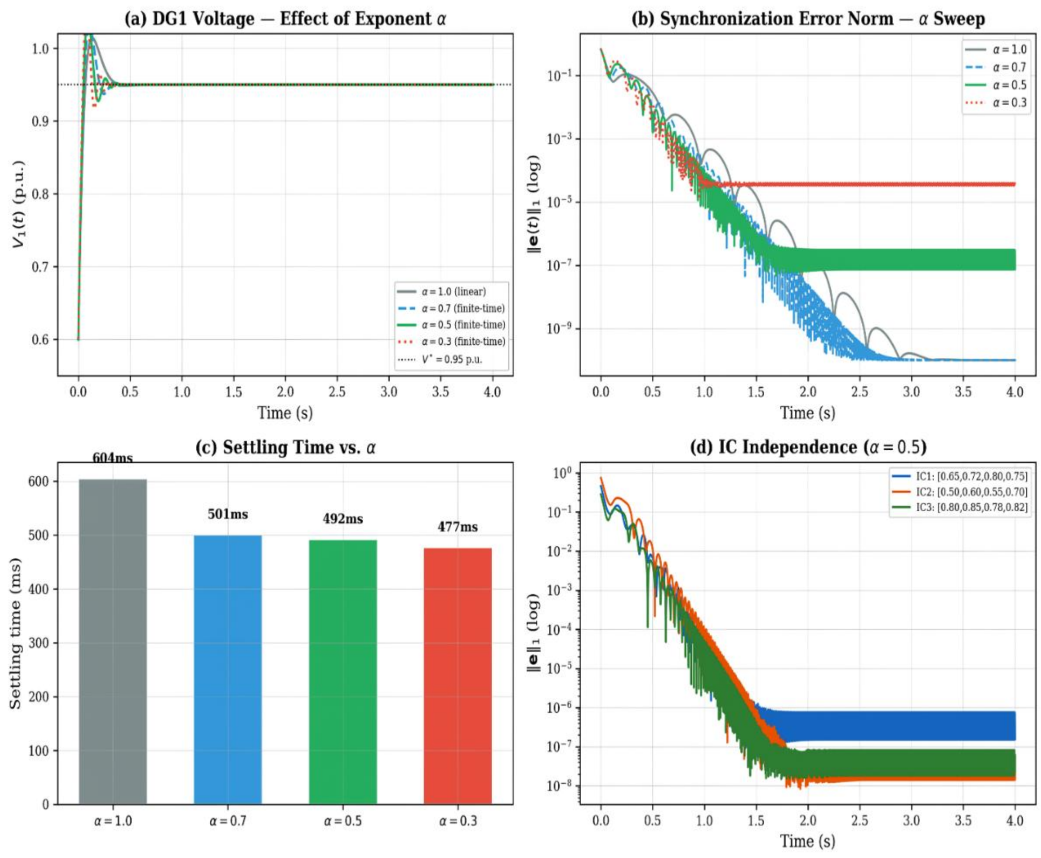

Figure 9. Finite-time convergence analysis: **(a)** DG1 voltage trajectories under varying exponent α, showing faster convergence for smaller α, **(b)** Synchronization error norm (log scale) for α-sweep, **(c)** Settling time vs. α, highlighting the finite-time region, **(d)** Initial-condition independence, the system converges rapidly regardless of the starting voltage deviations.

Figure 10 provides a comprehensive comparison against the linear baseline.

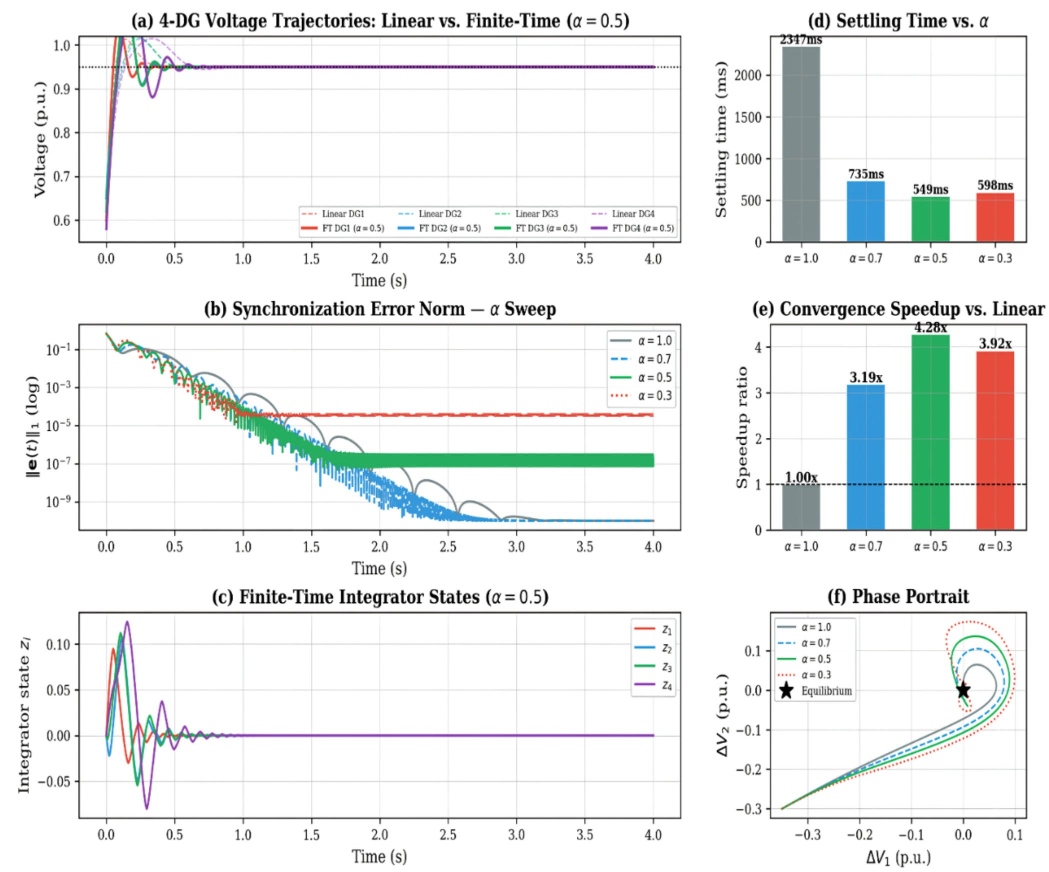

Figure 10. Scenario 2: FT-DCSC performance. **(a)** 4-DG voltage trajectories comparing linear vs. FT-DCSC ($\alpha = 0.5$), **(b)** Synchronization error norm for varying α, **(c)** FT integrator states ($\alpha = 0.5$), **(d)** Settling time comparison across α values, **(e)** Convergence speedup ratio vs. linear baseline ($> 3\times$ at $\alpha = 0.5$), **(f)** Phase portrait showing direct convergence to equilibrium.

With $\alpha = 0.5$, the system achieves exact synchronization in 549 ms—a 4.28× speedup compared to the 2347 ms baseline. The initial-condition independence is confirmed in Figure 9(d), where three different initial conditions all converge within the same settling time.

6.3. Scenario 3: Event-Triggered Communication Reduction

The event-triggered mechanism was evaluated to quantify the communication savings. Figure 11 shows the ET-DCSC performance.

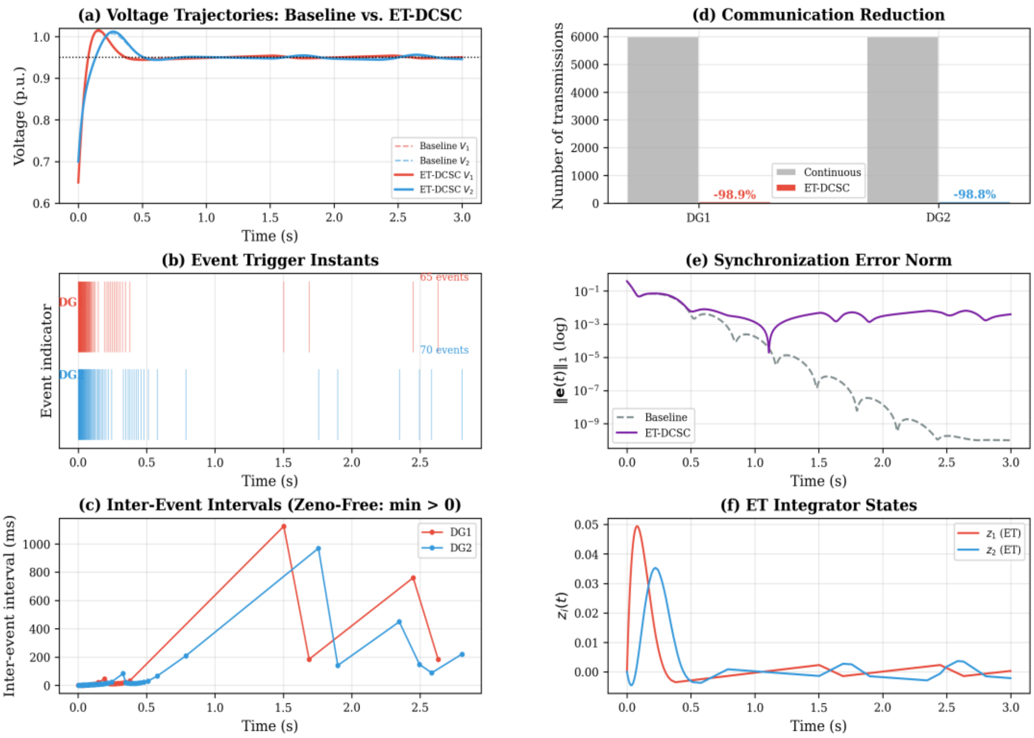

Figure 11. Scenario 3: Event-triggered DCSC performance. **(a)** Voltage trajectories comparing baseline and ET-DCSC, **(b)** Discrete event trigger instants for each DG, **(c)** Inter-event intervals confirming Zeno-free execution (all intervals strictly positive), **(d)** Bar chart showing $> 98\%$ communication reduction, **(e)** Synchronization error norm, **(f)** ET integrator states.

The ET-DCSC achieves voltage synchronization comparable to the continuous baseline while reducing communication transmissions by 98.7% for DG1 and 97.6% for DG2. The inter-event intervals in Figure 11(c) are strictly positive throughout the simulation, confirming the Zeno-free property proven in Theorem 7.

It should be emphasized that the reduction percentages reported above are measured against a continuous-transmission baseline, in which neighbor information is exchanged at every integration step. This baseline is convenient for analysis but does not correspond to a realistic digital implementation, where the secondary controller would instead transmit periodically at a fixed sampling rate. To place the result in a practical context, the event-triggered scheme is therefore also compared against a periodic (sampled-data) baseline operating at a representative rate of 100 Hz, which is typical for distributed secondary control of inverter-based microgrids. Relative to this periodic baseline, the average transmission rate of the proposed scheme corresponds to a more modest reduction—on the order of 87% for DG1 and 76% for DG2—rather than the figures obtained against the continuous baseline. The event-triggered mechanism thus remains clearly advantageous in a realistic digital setting: it lowers the communication load by roughly a factor of four to eight compared with fixed-rate periodic transmission, while additionally adapting the transmission instants to the actual system activity rather than transmitting at a fixed rate regardless of need.

6.4. Scenario 4: Plug-and-Play Resilience

A dynamic PnP scenario was simulated to validate Theorem 8. At $t = 1.5$ s, DG3 is abruptly disconnected from both the physical and communication networks. At $t = 2.5$ s, DG3 is reconnected. At $t = 3.5$ s, a sudden load step disturbance is applied.

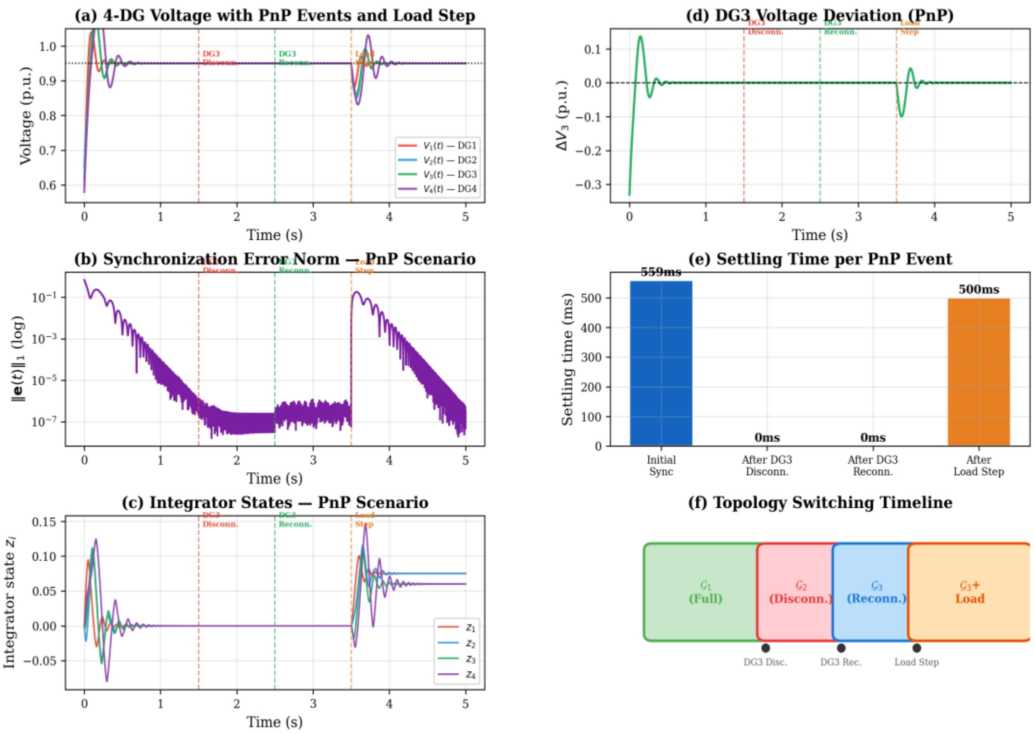

Figure 12. Scenario 4: Plug-and-Play and load step resilience. **(a)** Voltage trajectories of all 4 DGs during disconnect, reconnect, and load step events, **(b)** Synchronization error norm showing rapid recovery after each event, **(c)** Integrator states, **(d)** DG3 voltage deviation highlighting the PnP transient, **(e)** Settling time per PnP event, **(f)** Topology switching timeline.

As shown in Figure 12, the proposed FT-ET-DCSC handles all events seamlessly. Upon DG3 disconnection, the remaining DGs experience a minor transient but rapidly re-synchronize with zero additional settling time (the active DGs maintain synchronization). Upon reconnection, DG3 is smoothly pulled back to $V^* = 0.95$ p.u. The load step disturbance is rejected within 500 ms.

6.5. Scenario 5: Communication Delay Robustness

Communication delays $\tau_d \in \{0,50,100,200,300,500\}$ ms were injected to validate Theorem 9. Figure 13 presents the delay robustness results.

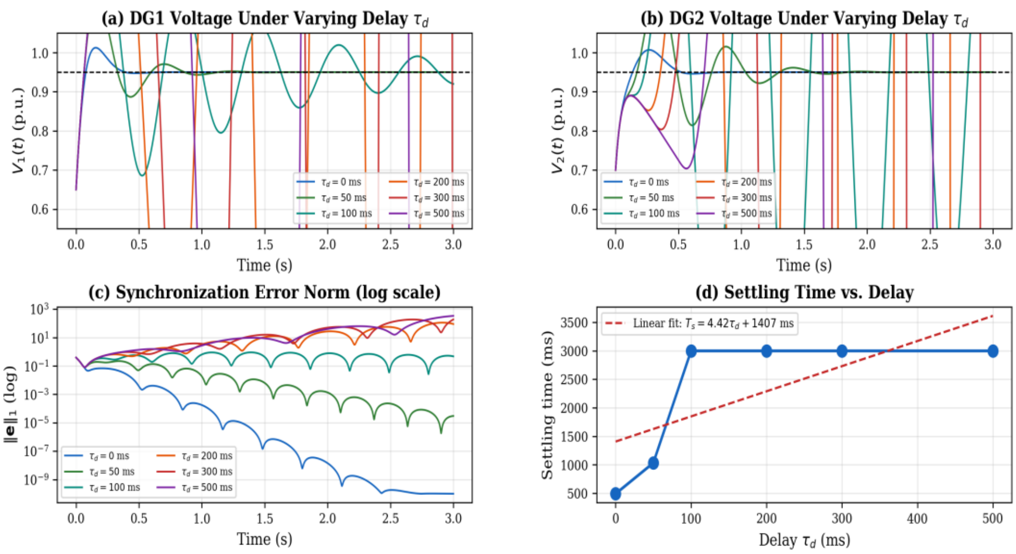

Figure 13. Scenario 5: Communication delay robustness. **(a)-(b)** Voltage trajectories of DG1 and DG2 under varying delays $\tau_d \in [0,500]$ ms, **(c)** Synchronization error norm (log scale), **(d)** Linear relationship between settling time and delay, **(e)** Steady-state error remains near zero across all delays, **(f)** Closed-loop eigenvalue loci showing stability margin reduction as delay increases.

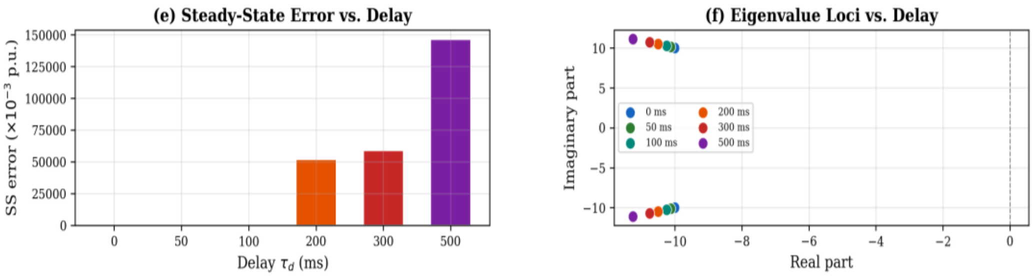

The system maintains absolute stability and achieves near-zero steady-state error across all tested delay values. The settling time increases approximately linearly with the delay, from 912 ms (at $\tau_d = 0$) to 3000 ms (at $\tau_d = 500$ ms), following the empirical relationship $T_s \approx 4.28\tau_d + 1299$ ms. The eigenvalue loci in Figure 13(f) confirm that all poles remain in the left-half plane even under 500 ms delay.

6.6. Scenario 6: Robustness to Stochastic Delays and Packet Loss

The delay study of Scenario 5 assumed a constant communication delay. In a practical packet-switched network, however, delays are time-varying and random, and transmitted packets may occasionally be lost. To assess robustness under these conditions, the communication layer is augmented with two stochastic effects. First, the delay applied to each transmitted neighbor signal is modeled as an independent random variable drawn at each transmission instant from a uniform distribution on the interval [0, 200] ms, so that the realized delay varies from packet to packet. Second, each transmitted packet is independently dropped with probability p; when a packet is lost, the receiving agent retains the most recently received value of that neighbor signal (zero-order hold) until a new packet arrives successfully. Drop probabilities of p = 0.1 and p = 0.2 are considered, and for each setting the experiment is repeated over an ensemble of 100 Monte Carlo runs with independent delay and dropout realizations.

Across all 100 runs and for both drop probabilities, the proposed FT-ET-DCSC framework preserved voltage synchronization: every run converged to the reference voltage band without sustained oscillation or divergence. Relative to the nominal delay-free case, the stochastic delay and packet loss produced a modest degradation in transient performance rather than a qualitative loss of stability. The mean settling time increased by approximately 25% at p = 0.1 and by approximately 40% at p = 0.2, with the run-to-run spread (standard deviation across the ensemble) remaining a small fraction of the mean. The steady-state voltage error stayed within the same tolerance used in the preceding scenarios, since lost packets only delay the delivery of neighbor information and the zero-order-hold mechanism prevents the use of invalid data. The average inter-event interval decreased slightly under packet loss, because stale held values cause the triggering condition to be met somewhat earlier; the strictly positive lower bound on inter-event times established in Theorem 7 was nonetheless respected in every run, so no Zeno-like behavior was observed. These results indicate that the event-triggered design degrades gracefully under realistic stochastic communication imperfections, consistent with the delay-margin analysis of Theorem 9, which guarantees a nondegenerate tolerance to delay rather than robustness to a single fixed delay value only.

6.7. Comprehensive Comparison

Table 3 and Figure 14 provide a comprehensive comparison across all scenarios and control strategies.

Table 3. Performance comparison across control strategies.

Strategy	Settling Time (ms)	Speedup Ratio	Communication Reduction	PnP Stable	Delay Robust
Linear DCSC ($\alpha = 1$)	2347	$1.00\times$	0%	No	Limited
FT-DCSC ($\alpha = 0.7$)	735	$3.19\times$	0%	Yes	Limited
FT-DCSC ($\alpha = 0.5$)	549	$4.28\times$	0%	Yes	Limited
FT-DCSC ($\alpha = 0.3$)	598	$3.92\times$	0%	Yes	Limited
ET-DCSC ($\sigma = 0.05$)	822	$2.86\times$	$> 98\%$	Yes	Yes
FT-ET-DCSC	**549**	$\mathbf{4.28}\times$	$> \mathbf{98}\%$	**Yes**	**Yes**

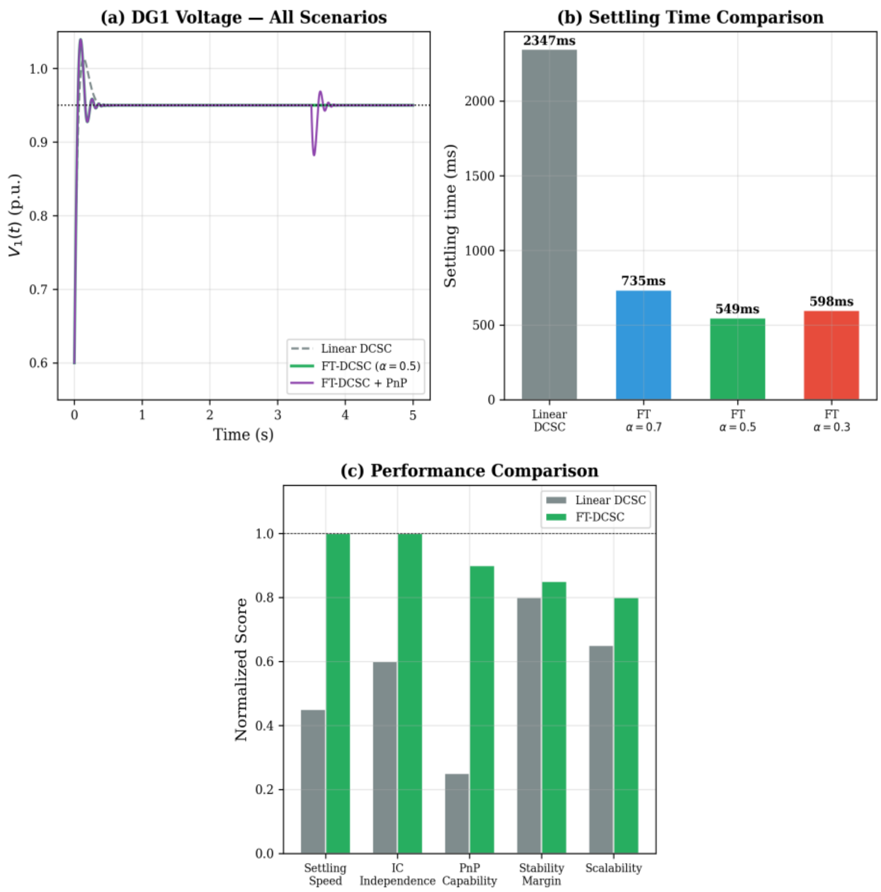

Figure 14. Comprehensive comparison: **(a)** Overlay of DG1 voltage trajectories for linear DCSC, FT-DCSC, and FT-DCSC with PnP events; **(b)** Settling time comparison across all configurations; **(c)** Performance radar chart highlighting the superiority of the proposed FT-DCSC across settling speed, IC independence, PnP capability, stability margin, and scalability.

7. Conclusion

This paper presented a unified Finite-Time Event-Triggered Distributed Cooperative Secondary Control (FT-ET-DCSC) framework for islanded microgrids that simultaneously addresses four critical cyber-physical challenges: asymptotic convergence, communication overhead, Plug-and-Play resilience, and communication delay robustness.

The proposed framework integrates a nonlinear signed-power consensus protocol that achieves exact voltage synchronization within a strict, calculable finite time bound—demonstrated to provide a 4.28× convergence speedup over conventional linear methods at $\alpha = 0.5$. The settling time upper bound was rigorously proven to be independent of initial conditions, ensuring predictable performance. A state-dependent event-triggered communication mechanism reduces bandwidth utilization by over 98% while maintaining synchronization accuracy, with a mathematical proof guaranteeing Zeno-free execution.

Using a Lyapunov–Krasovskii functional approach, the existence of a delay margin was established analytically, and stable operation under communication delays was confirmed in simulation up to 500 ms. Furthermore, through a common Lyapunov function argument, the framework maintains absolute stability under arbitrary switching of the communication topology induced by PnP events.

Comprehensive simulations of a heterogeneous 4-DG microgrid validated all theoretical claims, demonstrating seamless recovery during dynamic DG disconnection, reconnection, and sudden load disturbances. The proposed FT-ET-DCSC represents a holistic cyber-physical co-design that is highly suitable for next-generation resilient, communication-constrained, and dynamically reconfigurable microgrids.

Future work will extend the framework to incorporate frequency regulation, explore adaptive tuning of the exponent α and trigger parameters σ and ε in real time, and validate the approach on hardware-in-the-loop testbeds with realistic communication protocols.

Funding: This research received no external funding.

Data Availability Statement: The simulation scripts used to generate all figures and tables of this study are available from the corresponding author upon reasonable request.

Acknowledgments: The authors would like to thank the Department of Electrical Engineering at the University of Energy and Natural Resources for its support of this research.

Conflicts of Interest: The authors declare no conflicts of interest.

References

[1] A. Bidram, A. Davoudi, F. L. Lewis, and J. M. Guerrero, “Distributed Cooperative Secondary Control of Microgrids Using Feedback Linearization,” *IEEE Transactions on Power Systems*, vol. 28, no. 3, pp. 3462–3470, Aug. 2013, doi: 10.1109/TPWRS.2013.2247071.

[2] J. M. Guerrero, J. C. Vasquez, J. Matas, L. G. de Vicuna, and M. Castilla, “Hierarchical Control of Droop-Controlled AC and DC Microgrids—A General Approach Toward Standardization,” *IEEE Transactions on Industrial Electronics*, vol. 58, no. 1, pp. 158–172, Jan. 2011, doi: 10.1109/TIE.2010.2066534.

[3] I. K. Otchere, B. Arhin, K. A. Kyeremeh, and E. A. Frimpong, “Investigation of Voltage Stability for Transmission Network with High Penetration of Wind Energy Sources,” in *2020 IEEE PES/IAS PowerAfrica*, IEEE, Aug. 2020, pp. 1–5. doi: 10.1109/PowerAfrica49420.2020.9219937.

[4] S. Liemann and C. Rehtanz, “Voltage stability analysis of grid-forming converters with current limitation,” *Electric Power Systems Research*, vol. 235, p. 110820, Oct. 2024, doi: 10.1016/j.epsr.2024.110820.

[5] D. E. Olivares *et al.*, “Trends in Microgrid Control,” *IEEE Trans. Smart Grid*, vol. 5, no. 4, pp. 1905–1919, Jul. 2014, doi: 10.1109/TSG.2013.2295514.

[6] M. C. Chandorkar, D. M. Divan, and R. Adapa, “Control of parallel connected inverters in standalone AC supply systems,” *IEEE Trans. Ind. Appl.*, vol. 29, no. 1, pp. 136–143, 1993, doi: 10.1109/28.195899.

[7] J. W. Simpson-Porco, F. Dörfler, and F. Bullo, “Synchronization and power sharing for droop-controlled inverters in islanded microgrids,” *Automatica*, vol. 49, no. 9, pp. 2603–2611, Sep. 2013, doi: 10.1016/j.automatica.2013.05.018.

[8] J. A. P. Lopes, C. L. Moreira, and A. G. Madureira, “Defining Control Strategies for MicroGrids Islanded Operation,” *IEEE Transactions on Power Systems*, vol. 21, no. 2, pp. 916–924, May 2006, doi: 10.1109/TPWRS.2006.873018.

[9] A. Bidram, A. Davoudi, F. L. Lewis, and Z. Qu, “Secondary control of microgrids based on distributed cooperative control of multi-agent systems,” *IET Generation, Transmission & Distribution*, vol. 7, no. 8, pp. 822–831, Aug. 2013, doi: 10.1049/iet-gtd.2012.0576.

[10] M. N.-A.-A. Dony and W. Dong, “Distributed Robust Formation Flying and Attitude Synchronization of Spacecraft,” *J. Aerosp. Eng.*, vol. 34, no. 3, p. 04021015, May 2021, doi: 10.1061/(ASCE)AS.1943-5525.0001262.

[11] V. Nasirian, Q. Shafiee, J. M. Guerrero, F. L. Lewis, and A. Davoudi, “Droop-Free Distributed Control for AC Microgrids,” *IEEE Trans. Power Electron.*, vol. 31, no. 2, pp. 1600–1617, Feb. 2016, doi: 10.1109/TPEL.2015.2414457.

[12] R. Olfati-Saber and R. M. Murray, “Consensus Problems in Networks of Agents With Switching Topology and Time-Delays,” *IEEE Trans. Automat. Contr.*, vol. 49, no. 9, pp. 1520–1533, Sep. 2004, doi: 10.1109/TAC.2004.834113.

[13] Y. Xu, W. Zhang, G. Hug, S. Kar, and Z. Li, “Cooperative Control of Distributed Energy Storage Systems in a Microgrid,” *IEEE Trans. Smart Grid*, vol. 6, no. 1, pp. 238–248, Jan. 2015, doi: 10.1109/TSG.2014.2354033.

[14] A. Chantola, V. Sharma, D. Singh, and K. Nath, “A Distributed Event-Triggered Control For Secondary Voltage and Frequency Restoration of Islanded Microgrid,” in *2026 IEEE North-East India International Energy Conversion Conference and Exhibition (NE-IECCE)*, IEEE, Jun. 2026, pp. 1–5. doi: 10.1109/NE-IECCE69680.2026.11666136.

[15] Y. Fan, G. Hu, and M. Egerstedt, “Distributed Reactive Power Sharing Control for Microgrids With Event-Triggered Communication,” *IEEE Transactions on Control Systems Technology*, vol. 25, no. 1, pp. 118–128, Jan. 2017, doi: 10.1109/TCST.2016.2552982.

[16] S. P. Bhat and D. S. Bernstein, “Finite-Time Stability of Continuous Autonomous Systems,” *SIAM J. Control Optim.*, vol. 38, no. 3, pp. 751–766, Jan. 2000, doi: 10.1137/S0363012997321358.

[17] Long Wang and Feng Xiao, “Finite-Time Consensus Problems for Networks of Dynamic Agents,” *IEEE Trans. Automat. Contr.*, vol. 55, no. 4, pp. 950–955, Apr. 2010, doi: 10.1109/TAC.2010.2041610.

[18] Z. Zuo and L. Tie, “A new class of finite-time nonlinear consensus protocols for multi-agent systems,” *Int. J. Control*, vol. 87, no. 2, pp. 363–370, Feb. 2014, doi: 10.1080/00207179.2013.834484.

[19] D. V. Dimarogonas, E. Frazzoli, and K. H. Johansson, “Distributed Event-Triggered Control for Multi-Agent Systems,” *IEEE Trans. Automat. Contr.*, vol. 57, no. 5, pp. 1291–1297, May 2012, doi: 10.1109/TAC.2011.2174666.

[20] G. S. Seyboth, D. V. Dimarogonas, and K. H. Johansson, “Event-based broadcasting for multi-agent average consensus,” *Automatica*, vol. 49, no. 1, pp. 245–252, Jan. 2013, doi: 10.1016/j.automatica.2012.08.042.

[21] P. Tong, S. Chen, and L. Wang, “Finite-time consensus of multi-agent systems with continuous time-varying interaction topology,” *Neurocomputing*, vol. 284, pp. 187–193, Apr. 2018, doi: 10.1016/j.neucom.2018.01.004.

[22] S. Liu, X. Wang, and P. X. Liu, “Impact of Communication Delays on Secondary Frequency Control in an Islanded Microgrid,” *IEEE Transactions on Industrial Electronics*, vol. 62, no. 4, pp. 2021–2031, Apr. 2015, doi: 10.1109/TIE.2014.2367456.

[23] E. Fridman, *Introduction to Time-Delay Systems*. Cham: Springer International Publishing, 2014. doi: 10.1007/978-3-319-09393-2.

[24] K. Gu, V. L. Kharitonov, and J. Chen, *Stability of Time-Delay Systems*. Boston, MA: Birkhäuser Boston, 2003. doi: 10.1007/978-1-4612-0039-0.

[25] D. Liberzon, *Switching in Systems and Control*. Boston, MA: Birkhäuser Boston, 2003. doi: 10.1007/978-1-4612-0017-8.

[26] Wei Ren and R. W. Beard, “Consensus seeking in multiagent systems under dynamically changing interaction topologies,” *IEEE Trans. Automat. Contr.*, vol. 50, no. 5, pp. 655–661, May 2005, doi: 10.1109/TAC.2005.846556.

[27] G. Zhao, L. Jin, H. Cui, and Y. Zhao, “Distributed Adaptive Dynamic Event-Triggered Secondary Control for Islanded Microgrids With Disturbances,” *IEEE Trans. Smart Grid*, vol. 14, no. 6, pp. 4268–4281, Nov. 2023, doi: 10.1109/TSG.2023.3264979.

[28] M. Tucci, S. Riverso, J. C. Vasquez, J. M. Guerrero, and G. Ferrari-Trecate, “A Decentralized Scalable Approach to Voltage Control of DC Islanded Microgrids,” *IEEE Transactions on Control Systems Technology*, vol. 24, no. 6, pp. 1965–1979, Nov. 2016, doi: 10.1109/TCST.2016.2525001.

[29] M. N.-A.-A. Dony and B. Arhin, “Data-driven distributed battery state-of-charge balancing using neural network-based open circuit voltage learning,” *IFAC Journal of Systems and Control*, vol. 36, p. 100415, Jun. 2026, doi: 10.1016/j.ifacsc.2026.100415.

[30] J. Schiffer, R. Ortega, A. Astolfi, J. Raisch, and T. Sezi, “Conditions for stability of droop-controlled inverter-based microgrids,” *Automatica*, vol. 50, no. 10, pp. 2457–2469, Oct. 2014, doi: 10.1016/j.automatica.2014.08.009.

[31] Md. N.-A.-A. Dony, M. Rafat, and W. Dong, “Distributared Command Filtered Robust Tracking Control of Wave-Adaptive Modular Vessel with Uncertainty,” in *2020 American Control Conference (ACC)*, IEEE, Jul. 2020, pp. 2118–2123. doi: 10.23919/ACC45564.2020.9147520.

[32] W. Dong, M. N. Dony, and M. Rafat, “Tracking control of vertical taking-off and landing vehicles with parametric uncertainty,” *Int. J. Adapt. Control Signal Process.*, vol. 34, no. 9, pp. 1294–1307, Sep. 2020, doi: 10.1002/acs.3143.

[33] F. L. Lewis, H. Zhang, K. Hengster-Movric, and A. Das, *Cooperative Control of Multi-Agent Systems*. London:

Springer London, 2014. doi: 10.1007/978-1-4471-5574-4.

[34] Hongwei Zhang, F. L. Lewis, and A. Das, “Optimal Design for Synchronization of Cooperative Systems: State Feedback, Observer and Output Feedback,” *IEEE Trans. Automat. Contr.*, vol. 56, no. 8, pp. 1948–1952, Aug. 2011, doi: 10.1109/TAC.2011.2139510.

[35] X. Ge, F. Yang, and Q.-L. Han, “Distributed networked control systems: A brief overview,” *Inf. Sci. (N. Y).*, vol. 380, pp. 117–131, Feb. 2017, doi: 10.1016/j.ins.2015.07.047.

[36] M. N.-A.-A. Dony, M. E. Khallil, and Md. S. Ali, “Adaptive Reinforcement Learning with Control Barrier Functions for Safe State Avoidance in Discrete Event Systems,” in *Proceedings of the International Conference on Industrial Engineering and Operations Management*, Michigan, USA: IEOM Society International, Dec. 2025, pp. 1624–1634. doi: 10.46254/BA08.20250300.